

Drastic enhancement of high-order harmonic generation from endohedrally confined atoms

T. Topcu^{1*}, E. A. Bleda², and Z. Altun²

¹ *Department of Mathematics and Statistics, University of Nevada, Reno, Nevada 89557, USA*

² *Department of Physics, Marmara University, Goztepe Campus, Istanbul 34722, TURKEY*

(Dated: May 17, 2022)

Dynamically rich nature of the high-order harmonic generation process lends itself to a variety of ways to increase photon yield and extend the harmonic cut-off frequency. We show here that high-harmonic generation from an atom confined inside an attractive potential shell can show a dramatic increase in the photon yield in certain cases. We consider an endohedrally confined hydrogen atom inside a C_{60} cage as an example, and consider three distinct physical situations in which the initial state is (1) entirely confined inside the C_{60} , (2) partially outside, and (3) mainly localized on the cage wall. We demonstrate that when the atom-cage system starts in a state with a classical turning point outside the C_{60} shell, the high-harmonic photon yield can be enhanced up to 4 orders of magnitude when compared with a free atom in the same initial state. We explain the underlying physical mechanisms in each case using fully three-dimensional quantum simulations. This gives a prime example of how directly coupling an atom to a nanostructure can alter strong field processes in atoms in interesting ways.

I. INTRODUCTION

High-order harmonic generation (HHG) is a non-linear process in which an atom or a molecule interacts with an intense laser field and emits a broadband spectrum of photons. The photons are coherent harmonics of the driving laser field and have a relatively uniform intensity distribution forming a plateau. Similar intensities of the high-harmonics in the plateau region allow scientists to synthesize intense attosecond pulses of sub-femtosecond durations extending from the extreme ultraviolet to the soft X-ray region. These spatially and temporally coherent pulses open up the possibility of developing new techniques for understanding the underlining dynamics of physical and chemical changes that occur in atomic and molecular systems at femtosecond and attosecond timescales [1–4].

Composing such short pulses in a meaningful way requires the high-harmonic photons to also have sufficiently large intensities. Efforts to increase high-harmonic photon intensities while increasing the harmonic cut-off has therefore drawn effort. Such techniques range from invoking many-electron effects [5, 6] to exploiting phase matching in macroscopic targets [7–10]. Another method exploits this by using nanometer size metal tips to increase the electric field felt by tunneled electrons in a way to shift the scales in favor of the recombination process. A nanostructure is used to enhance the HHG yield in this case, although the atom itself is not directly coupled to it [11–14]. In this paper, we take a first step in this direction by directly coupling an atom to a nanostructure to alter the tunneling and recombination dynamics. We investigate possible ways in which the highly nonlinear HHG process can be modified to give increased photon yield to aid in the production of higher intensity pulses.

The physical mechanism behind HHG can be modeled as a three-step process [15]: (1) the electric field of the laser suppresses the Coulomb potential which allows the electron to tunnel into the continuum. (2) The laser field accelerates the free electron. When the sign of the electric field changes, the electron accelerates towards the parent ion. (3) Finally, the electron recombines with the parent ion and emits a photon with an energy that is equal to the sum of the binding energy and the kinetic energy gained during the propagation step (2). By coupling the atom to a fullerene cage, we demonstrate that the dynamics in all these steps can be modified in interesting, and in some cases, useful ways.

In this study, we investigate high-order harmonic generation (HHG) from a hydrogen atom confined inside a fullerene, specifically, C_{60} . We solve the time-dependent Schrödinger equation (TDSE) within a single active-electron model to investigate three physically distinct situations: (1) when the atom is initially prepared in the ground state which is entirely confined inside the fullerene cage, (2) in the $2s^*$ state of the combined atom-fullerene system, in which the expectation value $\langle r \rangle$ falls inside the cage wall, and finally (3) in the $3s^*$ state with the classical turning point outside the fullerene wall. In each of these cases, we identify the most likely position of the electron with the expectation value $\langle r \rangle$ at $3n^2/2$, which is before the classical turning point at $2n^2$. When the atom starts in the ground state, we find that confinement introduces some enhancement in the photon yield when compared with that from a free atom, which is lost when we moderately increase the laser intensity. Initially preparing the combined atom-fullerene system in the first excited state ($2s^*$) results in a dramatically reduced cut-off frequency, which although undesirable, exhibits interesting physics. In this case, the electron is mainly localized on the C_{60} cage, and we elucidate the physical mechanism at play using avoided crossings. Finally, we show that by preparing the atom in an excited state

* ttopcu.unr@gmail.com

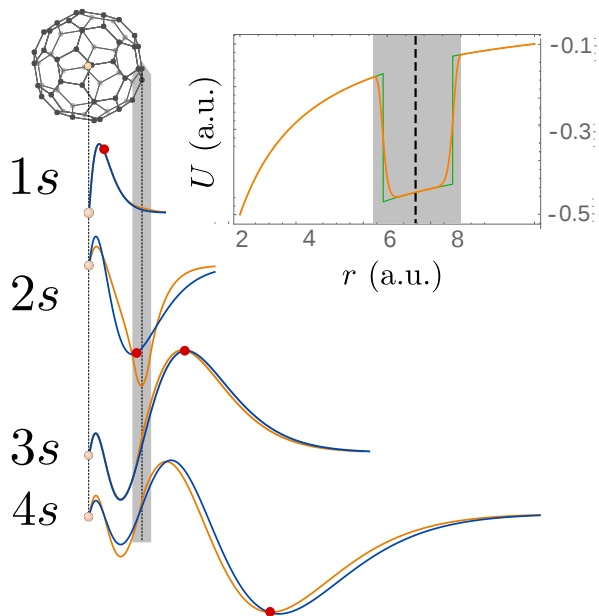


FIG. 1. (Color online) Relative size scales involved in the harmonic generation from Ry atoms confined inside a C_{60} molecule. The model potential commonly used to describe a C_{60} molecule is a spherical potential shell with a radius of 6.84 a.u. The panel on the right shows the combined Coulomb potential and the model potential for the C_{60} molecule (solid green). In our simulations, we use the model seen as the solid orange curve. The eigenstates listed compare free atom (solid blue) and confined atom (solid orange) states, which we use as initial states in our simulations. The red points on the free atom eigenstates indicate $\langle r \rangle = 3n^2/2$.

with a classical turning point outside the fullerene shell, the photon yield can be dramatically enhanced while retaining the same cut-off frequency when compared with the free atom. We attribute this to an afocal lensing effect mediated by the spherically symmetrical potential of the fullerene cage and present momentum- and spatial distribution of the time-dependent wave function.

We start by giving a brief account of our three-dimensional time-dependent simulations and the model we use to describe the atom-fullerene system in the laser field. In Sec. III, we present results from our simulations and explain the underlying mechanisms based on our time-dependent simulations (Sec. III A and III C) and in terms of avoided crossings (Sec. III B). We conclude in Section IV by suggesting some possible future directions.

II. SIMULATIONS

All of our simulations are based on *ab initio* solutions of the three-dimensional time-dependent Schrödinger equation (TDSE) in the length gauge. Detailed accounts of our simulations can be found spread over several papers, such as in [16] and [17]. Here we only give a concise de-

scription of our methods emphasizing details most pertinent to present calculations. We start with numerical solutions of the TDSE. We then describe how we model the fullerene cage and describe a Green's function method for visualizing the wave function in space. We also perform calculations of the momentum space wave function to gain further insight into the dynamics, which we describe in Sec. II D.

A. Fully three-dimensional TDSE

We carry out three-dimensional quantum calculations by solving the time-dependent Schrödinger equation [18]. We decompose the time-dependent wave function in spherical harmonics $Y_{\ell,m}(\theta, \phi)$ as

$$\Psi(\vec{r}, t) = \sum_{\ell=0}^{L_m} f_{\ell}(r, t) Y_{\ell,m}(\theta, \phi). \quad (1)$$

The time-dependence is captured in the coefficient $f_{\ell}(r, t)$ discretized on a square-root mesh in the r -direction for each angular momenta. This is ideal for describing Rydberg states because it places approximately the same number of radial points between the nodes of an eigenstate. On this grid, the Schrödinger equation is

$$\left[i \frac{\partial}{\partial t} - H(r, l, t) \right] \psi(r, l, t) = 0. \quad (2)$$

We split the total hamiltonian into an atomic hamiltonian plus the interaction hamiltonian: $H(r, l, t) = H_A(r, l) + H_L(r, t) - E_0$, where we subtract the initial state energy from the total hamiltonian to reduce the numerical phase accumulation over time. The atomic hamiltonian H_A and the hamiltonian describing the interaction of the atom with the laser field in the length gauge are

$$H_A(r, l) = -\frac{1}{2} \frac{d^2}{dr^2} - \frac{1}{r} + \frac{l(l+1)}{2r^2} \quad (3)$$

$$H_L(r, t) = F(t)z \cos(\omega t). \quad (4)$$

We use the lowest order split operator technique to evolve the total wavefunction in time according to (2), where each split piece is propagated using an $\mathcal{O}(\delta t^3)$ implicit scheme, which is an exactly unitary propagator. A detailed account of the $\mathcal{O}(\delta t^3)$ implicit method and the split operator technique we use is given in [18].

We report Fourier transform of the dipole acceleration, $a(t) = \langle \ddot{z} \rangle(t)$, in our results since the radiated power in the length gauge is proportional to the square of the dipole acceleration: $S(\omega) = 2\omega^4 |a(\omega)|^2 / (3\pi c^3)$. We also calculate the dipole moment $\langle z \rangle(t)$ and the dipole velocity $\langle \dot{z} \rangle(t)$ along with $a(t)$ for comparison. The level of agreement between these forms gives us an idea about how strong the laser pulse is since $\langle z \rangle(t)$, $\langle \dot{z} \rangle(t)$, and $a(t)$ agree well when the pulse is effectively weak, and start to

differ as one moves further into the strong field regime. The time-dependent dipole acceleration is given by

$$a(t) = -\langle \psi(r, t) | [H, [H, z]] | \psi(r, t) \rangle. \quad (5)$$

We keep track of the time-dependent ionization probability, $P(t)$, as well, and the total probability amplitude inside the box not bound to an eigenstate of the atom-fullerene system, $\tilde{P}(t)$, through the remaining norm inside our spatial box:

$$P(t) = 1 - \int_0^R |\psi(r, t)|^2 dr, \quad (6)$$

$$\tilde{P}(t) = \int_0^R |\psi(r, t)|^2 dr - \sum_{n,\ell} \left| \int_0^R \phi_{n,\ell}(r) \psi(r, t) dr \right|^2. \quad (7)$$

Here R is the radial extent of the box, and $\phi_{n,\ell}(r)$ are the eigenstates of H_A . Note that $\tilde{P}(t) \rightarrow 0$ in the long-time limit because the sum in (6) is performed over a complete set of states inside the box.

We use an 800 nm laser at an intensity of 5×10^{13} W/cm² for the simulations of HHG out of the ground state. The pulse duration, in this case, is 4-cycles, which corresponds to a ~ 10 fs pulse at FWHM. The intensity is chosen to be below the saturation intensity of the first charge stage of C₆₀ at 800 nm [19]. On the other hand, multiphoton ionization and fragmentation processes can still take place in intensities below the saturation limit, beyond which the fullerene molecules are completely destroyed, and a hot carbon plasma is created. In this regime, ionization stage rarely goes beyond C₆₀²⁺ due to competition between the C₆₀ lattice modes and electron emission, and fragmentation takes place by emission of C_{60-2m}^{q+} fragments where $m = 0, 1, \dots$ and $q = 1, 2, 3$ [20] in the intensity range $10^{13} - 10^{14}$ W/cm² at 790 nm. In this case, fragmentation takes place via multiphoton excitation of a giant plasmon resonance at ~ 20 eV and is a perturbative process at these intensities [20].

Another physical process we ignore is HHG from the C₆₀ molecule itself [21]. The overall dielectric response of the C₆₀ molecule is dominated by the collective motion of the π -electrons and the large electron density relative to the Debye length leads to efficient screening of the laser field inside the molecule [20]. Fields even stronger than what we consider here would be hardly felt by the electrons in the interior of the molecule, and no efficient tunneling takes place from the C₆₀ molecule. The fullerene will ionize and fragment long before tunneling can take place to start an efficient HHG process.

When simulating HHG from excited states, we scale the wavelength and the intensity as $800n^3$ nm and $(1.5/n^8) \times 10^{14}$ W/cm² to keep the time-dependent dynamics in the same physical regime throughout the simulations involving Ry states. These laser frequencies and intensities are far below those that would cause structural changes in the C₆₀ molecule for $n \geq 2$.

B. The model potential

We place the H atom at the center of a spherically symmetric potential shell centered at the position of the atomic nucleus ($r = 0$). In our simulations, we smooth out the sharp edges of this model potential to prevent artificial high-frequency components from appearing in the harmonic spectra (solid orange curve in Fig. 1). We model the C₆₀ cage as

$$U_{C_{60}}(r) = U_0 \exp\left(-\frac{(r - r_c)^{10}}{a}\right), \quad (8)$$

where U_0 is the depth and r_c is the distance from the nucleus to the center of the shell. The parameter a , which is associated with the width of the cage, is found by least square fitting the above form to the following radial square-well potential for the C₆₀ structure [22]:

$$U_{C_{60}}(r) = \begin{cases} -0.3 & 5.89 \leq r \leq 7.78 \\ 0 & \text{otherwise} \end{cases} \quad (9)$$

We find the parameter a in (8) to be 0.83 (a.u.)¹⁰. We repeated few of our calculations using the model potential in Eq. (9) and found no significant difference relative to the harmonic spectra generated using (8) below the harmonic cut-off frequency. To differentiate the bound states of the H atoms from the those of the atom-fullerene system, we indicate the bound states of the confined atom with an asterisk, *i.e.* 1s*, 2s*, 3s*, whereas corresponding atomic states are labeled 1s, 2s, and 3s. We use atomic units throughout unless we explicitly indicate otherwise.

C. Green's function method

To demonstrate the physical mechanism behind the enhancement, we see when the atom-fullerene system starts in the 3s*@C₆₀ state, we observe the time-dependent behavior of the probability amplitude near the fullerene cage. Discerning details of the interesting dynamics of the wave function near the fullerene wall is however difficult using the fully three-dimensional simulations we describe in Sec. II A. The reason is that most of the initial wavefunction remains unperturbed by the driving laser field, and the part of the wavefunction that takes part in the interesting dynamics that generate high-harmonic photons gets buried underneath the initial wavefunction making it difficult to see. To observe the behavior of the wavefunction that contributes to the HHG process, we, therefore, employ a time-dependent method similar to the first-order time-dependent perturbation theory which we briefly describe below. Details of this method can be found, *e.g.*, in [16].

We use a time-dependent method similar to the first-order time-dependent perturbation theory. We split the total Hamiltonian of the system into two pieces H_A and H_L as before (3). We express the total wavefunction as a superposition of the initial state, and the time-dependent

correction, $\psi(r, l, t) = \psi_0(r, l) + \psi_1(r, l, t)$, and write the time-dependent Schrödinger equation as

$$\left[i \frac{\partial}{\partial t} - H(r, l, t) \right] \psi_1(r, l, t) = H_L \psi_0. \quad (10)$$

Here $H_L(r, t)\psi_0(r, l)$ acts as a source term. This method is particularly useful when the amplitude in $\psi_1(t)$ is much smaller than the amplitude in ψ_0 as is the case in our simulations. The wave function $\psi_1(t)$ is initially zero everywhere, and it encodes the time-dependent corrections to the unperturbed wave function ψ_0 . This method allows for atomic processes of all orders, such as tunneling, as well as single- and multi-photon processes.

D. Momentum distribution

To assess the underlying physical mechanism responsible for enhancement when the atom starts in an excited state with a classical turning point outside the fullerene cage ($\text{H}(3s^*)@C_{60}$), we also calculate the time-dependent momentum distribution of the wavefunction. We evaluate the momentum distribution following the procedure outlined in Ref. [23] with the exception that it is the momentum distribution of the total wavefunction and not just the escaping amplitude. For the sake of completeness, we briefly describe the method here. During the time evolution of Eq. (2), the ionized part of the wave function is removed from the box after every time step to prevent unphysical reflections from the radial box edge. This is done using a mask function $\mathcal{M}(r)$, spanning the final 1/3 of the radial box. The removed part of the wavefunction is

$$\Delta\psi_l(r, t') = [1 - \mathcal{M}(r)] \psi_l(r, t'), \quad (11)$$

and we evaluate $\Psi_l(r, t') = \psi_l(r, t') + \Delta\psi_l(r, t')$. In order to emphasize the momentum distribution beyond the peak of the depressed Coulomb potential beyond $r > 1/\sqrt{F_p}$, we apply a mask function to $\Psi_l(r, t')$ in the region $r < 1/\sqrt{F_p}$ which exponentially suppresses the wavefunction as $r \rightarrow 0$. Here F_p is the peak electric field of the laser pulse. We then Fourier transform $\Psi_l(r, t')$ to obtain the momentum space wave function $\phi(p_\rho, p_z, t')$,

$$\begin{aligned} \phi(p_\rho, p_z, t') &= 2 \sum_l (-i)^l Y_{l,m}(\theta, \varphi) \\ &\times \int_0^\infty j_l(pr) \Psi_l(r, t') r^2 dr. \end{aligned} \quad (12)$$

Here the momentum is $p = (p_\rho^2 + p_z^2)^{1/2}$ and $j_l(pr)$ are the spherical Bessel functions. We then evolve $\phi(p_\rho, p_z, t')$ to a later time t using the semi-classical propagator,

$$\phi(p_\rho, p_z, t) = \phi(p_\rho, p_z, t') e^{-iS} \quad (13)$$

where S is the classical action. Given the time-dependent laser field $F(t)$, action S is calculated numerically by in-

tegrating p_z^2 along the laser polarization,

$$S = \frac{1}{2} p_\rho^2 (t - t') + \frac{1}{2} \int_{t'}^t p_z^2 dt'', \quad (14)$$

$$p_z = \int_{t'}^t F(t'') dt''. \quad (15)$$

We are assuming that the ionized electron is freely propagating in the classical laser field in the absence of the Coulomb field of its parent ion. Because the laser field is polarized along the z -axis, p_ρ is the perpendicular component of the wavepacket p_\perp to the laser polarization, whereas p_\parallel is p_z .

III. RESULTS

We consider the following three distinct situations: (1) when the initial state of the combined atom-fullerene system is entirely confined inside the cage ($\text{H}(1s^*)@C_{60}$), (2) when $\langle r \rangle = 3n^2/2$ falls in the fullerene wall ($\text{H}(2s^*)@C_{60}$), and (3) when the classical turning point is outside the cage wall ($\text{H}(3s^*)@C_{60}$). In the $1s^*$ state, the classical turning point is well inside the cage. We observe ~ 4 orders of magnitude enhancement in yield in case (3) for the $3s^*$ state. Finally, we see a drastic reduction in cut-off in case (2) – although not desirable for applications – displays interesting physics when we vary the cage depth due to the existence of avoided crossings.

A. $\text{H}(1s^*)@C_{60}$

The upper panel of Fig. 2 compares HHG spectra from a free and a confined H atom inside the C_{60} fullerene when the atom and the combined atom-fullerene system is initially prepared in their respective ground states $1s$ and $1s^*$. The laser intensity and the wavelength in this figure are 5.0×10^{13} W/cm² and 800 nm. In the ground state of the $\text{H}@C_{60}$ system, $2n^2 < r_c$ and the radial wavefunction is entirely confined inside the fullerene cage. This results in bound state energies for the free and the confined systems being the same within one part in 10^5 .

Comparing spectra in the dipole, velocity and acceleration forms, we find that all gauges agree well throughout the plateau region except at low harmonics below $\omega/\omega_0 \lesssim 6$. In this low harmonic region, $\langle z \rangle$ and $\langle \dot{z} \rangle$ agree well and larger than $\langle \ddot{z} \rangle$ by a factor 100. Additionally, the ionization probability after the laser pulse is well below a percent for the free atom and $\sim 4\%$ for the $\text{H}(1s^*)@C_{60}$ system. Low ionization probabilities combined with good agreement between different gauges in most of the plateau region suggests that we are in the weak and short pulse regime in the top panel of Fig. 2 [17, 24], where macroscopic effects due to depletion and dispersion due to free electrons from the ionized atoms would be negligible.

The enhancement in the upper panel of Fig. 2 goes away when we increase the intensity using the same wavelength in the second panel of Fig. 2 where the intensity is three times larger than that in the top panel at 1.5×10^{14} W/cm². The enhancement in the HHG yield in the upper panel when the intensity is 5.0×10^{13} W/cm² is due to the fact that the Coulomb barrier which the electron needs to tunnel in the second step of the HHG process is partially reduced for ~ 2 a.u. inside the classically forbidden region. This increases the tunneling probability compared the free atom for which the binding energy of the initial state is the same. When the laser intensity is increased, however, this reduction in the Coulomb barrier becomes less important because the potential barrier is further suppressed. In this case, the momentum component of the returning wave packet parallel to the laser polarization, p_{\parallel} , dominates more over the perpendicular component p_{\perp} and we approach the regime in which there is little boost to the tunneling probability by confining the atom inside the fullerene. In this case, the fullerene cage provides to net lensing effect to decrease the spatial spread of the recombining wave packet; therefore there is no net increase in the recombination probability. In this case, the enhancement we see in the upper panel of Fig. 2 goes away in the lower panel where the laser is more intense.

The C₆₀ shell acts like an afocal lens (also called a zero meniscus lens) for both the outgoing (tunneling) and the incoming (recombining) wave packets at the first and third steps of the HHG process. Such a lens has an infinite focal length, meaning it neither focuses nor diverges the beams. However, it squeezes or spreads the rays without changing their direction (See Fig. 3). If the rays are incoming (as in the figure), they are squeezed together, and if they are outgoing (reverse the directions of the rays in the figure) they spread out, without changing direction.

For HHG out of the 1s* ground state, the classical turning point is at $2n^2 = 2$ a.u., which is inside the C₆₀ cage. This means tunneling happens inside and the outgoing wave packet spreads out as it exits the cage. After it is turned around and driven back to the atom for recombination, now the incoming wavepacket is bunched together again before it recombines. As a result, both the outgoing and the incoming wavepackets have the same spread and the momentum distribution, there is nothing different happening compared to when the electron was not confined, and we do not see any difference in the emission spectra (see Fig. 3).

There are two crucial points to note here: First, tunneling happens near the classical turning point at $2n^2$, and the recombination occurs near the nucleus. The latter is because momentum, as well as energy, must be conserved for the electron to emit a photon. The second crucial point is that the incoming wavepacket mainly recombines into the state out of which it initially tunneled (we had shown this our Rydberg HHG paper).

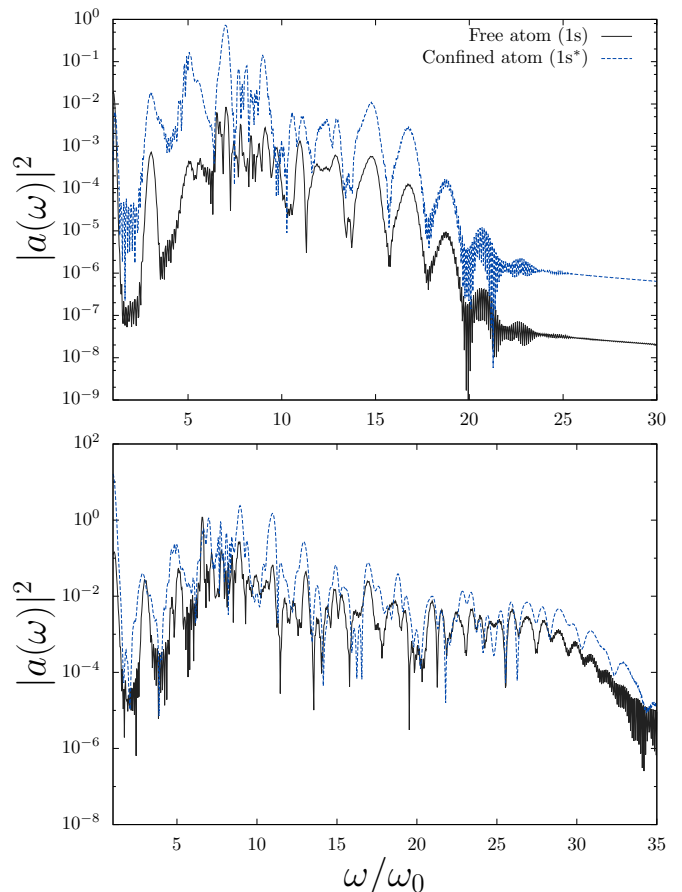


FIG. 2. (Color online) The upper panel compares HHG spectra from a free (solid black) and a confined (dashed blue) H atom initially prepared in the ground state. The laser intensity is 5.0×10^{13} W/cm² and the wavelength is 800 nm. In this case, yield from the combined atom-fullerene system is roughly an order of magnitude larger than the yield from a free H atom alone. This enhancement, however, goes away when the intensity is increased, which is shown in the lower panel in which the laser intensity is 1.5×10^{14} W/cm².

B. H(2s*)@C₆₀

The upper panel of Fig. 4 shows HHG spectra when the atom and the combined atom-fullerene system is initially prepared in their first excited states 2s and 2s*. The laser intensity and the wavelength in this figure are $5.0 \times 10^{13}/n^8$ W/cm² and $800n^3$ nm where $n = 2$. In the 2s* state of the H@C₆₀ system, $(3/2)n^2 = 6$ a.u. and $\langle r \rangle$ falls inside the wall of the fullerene cage (8). As a result, the bound state energy of the 2s* state is significantly more deeply bound at -0.239 a.u. than the 2s state at -0.125 a.u. In this case, we see a drastic reduction in the cut-off harmonic in the spectrum of the combined atom-fullerene system at $\omega/\omega_0 < 10$ compared to the spectrum from the free H atom at $\omega/\omega_0 \sim 54$. Although a reduction in the cut-off frequency is not something practically desirable, we will show below that it follows from interesting physics

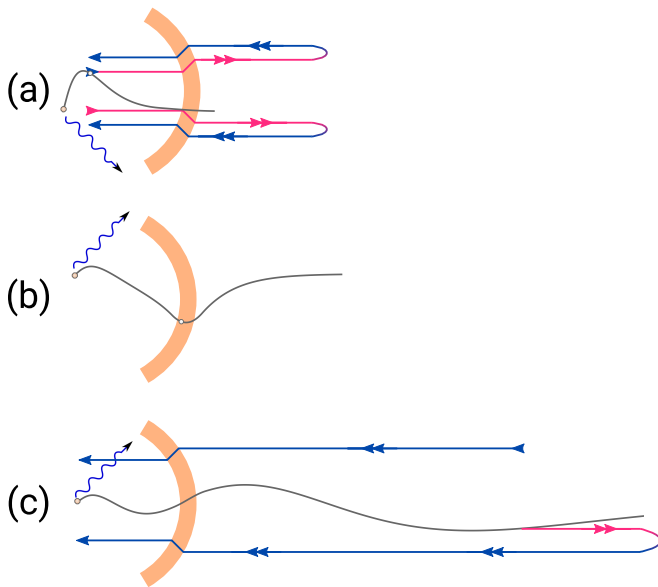


FIG. 3. (Color online) The afocal lensing effect discussed in the paper leading to three different situations when the combined atom system is initially prepared in: (a) the ground state where both tunneling and recombination takes place inside the fullerene cage, (b) the $2s^*$ state when electron is mainly localized on the fullerene wall, and (c) the $3s^*$ state where the tunneling happens outside the cage but the recombination takes place inside.

and one can turn the HHG plateau on and off by changing the depth of the confining potential.

In the case of the free H atom, the dipole and velocity form of the emitted power agree well everywhere except at low harmonics below $\omega/\omega_0 \lesssim 10$ where they differ by about a factor of 100. The dipole acceleration $\langle \ddot{z} \rangle$ is, however, smaller than $\langle \dot{z} \rangle$ by about two orders of magnitude throughout the entire free atom spectrum. Everything happens in the low harmonic region $\omega/\omega_0 \lesssim 10$ when the atom is confined, where $\langle \dot{z} \rangle$ is larger than $\langle \ddot{z} \rangle$ by two orders of magnitude. On the other hand, there is practically no ionization from either of the two systems by the end of the laser pulse. No ionization means the reduction in the cut-off for the H@C₆₀ system does not follow from depletion. In fact, we see that $\omega/\omega_0 \lesssim 10$ is the region in which HHG spectrum the spherically symmetric cage potential (8) resides in the absence of the H atom when the fullerene model is prepared in its only bound state. This spectrum is shown in the bottom panel of Fig. 4 where the depth of the C₆₀ shell is adjusted so that its ground state energy matches the energy of the H($2s^*$)@C₆₀ system. Both spectra show strong harmonics below $\omega/\omega_0 \lesssim 5$, which can be understood within a picture based on avoided crossings as we explain below.

In the context of Fig. 3, the wave function is mainly localized on the C₆₀ wall, and the depressed potential is narrower compared to the situation in which it is localized where $1s^*$ state resides. The radial wave func-

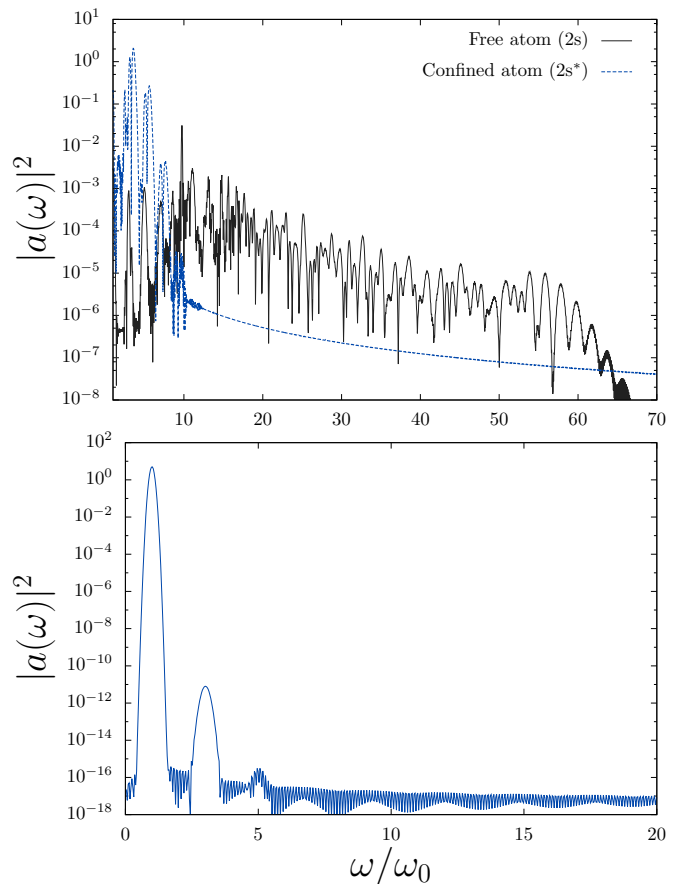


FIG. 4. (Color online) The top panel compares HHG spectra from a free H atom in the $2s$ state (black solid) with that from an atom confined inside the C₆₀ fullerene when the combined atom-fullerene system is in the first excited state $2s^*$ (blue dotted). In the confined atom case, the cut-off is reduced by about a factor of 6 because the $2s^*$ state is radially localized on the fullerene cage wall. The bottom panel shows the spectrum from the ground state of the spherically symmetric shell potential (8) in the same laser field with the depth adjusted so that its initial ground state has the same binding energy as the $2s^*$ state of the atom-fullerene system. In these simulations, the laser intensity and the wavelength are $5.0 \times 10^{13}/n^8$ W/cm² and $800n^3$ nm where $n = 2$.

tion can be seen in the top panel of Fig. 6. Before the avoided crossing in Fig. 5, the $2s^*$ state is localized on the fullerene cage wall and can tunnel through to either the left or the right of the potential barrier. It will tunnel to the left of the barrier towards the atomic core more preferentially, because of the asymmetric shape of the depressed Coulomb barrier in which it sits. This substantially reduces the tunneling amplitude for the electron wave packet that can effectively contribute to the HHG process, which requires a long excursion in the laser field before recombination. This accounts for the much shorter cut-off harmonic seen on the top panel of Fig. 4 for the $2s^*$ initial state when compared with the spectrum from the free atom that starts in $2s$ state. Note that the $2s^*$

state is more deeply bound at ~ -0.24 a.u. than the 2s state at ~ -0.125 a.u., which by itself cannot account for the factor of ~ 6 reduction in cut-off frequency.

To understand the reduction in cut-off seen in Fig. 4, we will start by describing a simple 2-level picture to analyze the 1s and 2s energy levels. We examine the energy shifts induced by the confining potential based on the relative strengths of the matrix elements.

The total Hamiltonian is $H = H_a + U_c$, where H_a and U_c are the atomic hamiltonian and the cage potential. Considering only the two lowest energy levels of hydrogen, the matrix representation of H in the eigenbasis of H_a is

$$\begin{pmatrix} E_1 & 0 \\ 0 & E_2 \end{pmatrix} + \begin{pmatrix} W_1 & W \\ W^* & W_2 \end{pmatrix} = \begin{pmatrix} E_1 + W_1 & W \\ W^* & E_2 + W_2 \end{pmatrix}. \quad (16)$$

Here the first term on the left represents the unperturbed atom whereas the second term is the confining potential. The matrix elements are: $E_1 = \langle 1s | H_a | 1s \rangle$, $E_2 = \langle 2s | H_a | 2s \rangle$, $W_1 = \langle 1s | U_c | 1s \rangle$, $W_2 = \langle 2s | U_c | 2s \rangle$, and $W = \langle 1s | U_c | 2s \rangle$. Diagonalizing this Hamiltonian results in the following eigenvalues:

$$E_{\pm} = \frac{1}{2}(E_1 + E_2 + W_1 + W_2) \pm \frac{1}{2} [(E_1 - E_2 + W_1 - W_2)^2 + 4|W|^2]^{1/2}, \quad (17)$$

which are the energies of the confined atom. The matrix elements W_1 , W_2 and W depend on the potential depth U_0 as well as the position and width of the cage wall:

$$W_1 = U_0 \int_{\Omega} \int_{r_1}^{r_2} |\phi_{1s}(\mathbf{r})|^2 d^3\mathbf{r}, \quad (18)$$

$$W_2 = U_0 \int_{\Omega} \int_{r_1}^{r_2} |\phi_{2s}(\mathbf{r})|^2 d^3\mathbf{r}, \quad (19)$$

$$W = U_0 \int_{\Omega} \int_{r_1}^{r_2} \phi_{1s}^*(\mathbf{r}) \phi_{2s}(\mathbf{r}) d^3\mathbf{r}. \quad (20)$$

Although the radial part of the integrals are over the range $r \in [r_1, r_2]$, angular integrals are evaluated over the entire 4π solid angle since the potential is spherically symmetric. This decouples states with different parity, such as $2s^*$ and $2p^*$, and $W_{2s^*, 2p^*} = 0$. As a result, the hamiltonian in Eq. (16) becomes diagonal with eigenvalues $E_1 + W_1$ and $E_2 + W_2$.

From Eq. 17, the energies E_+ and E_- can only become equal when

$$E_1 - E_2 + W_1 - W_2 = 0, \quad (21)$$

$$W = 0, \quad (22)$$

simultaneously. A non-vanishing off-diagonal matrix element prevents the energies from becoming equal for any value of the parameter U_0 . In this case we observe an avoided crossing as we show below.

Even though radial wavefunctions for the $1s^*$ and $2s^*$ states are orthogonal, we are only integrating over r

within the wall. It is clear in Fig. 1 that both states have non-vanishing amplitudes inside the wall. Therefore none of the matrix elements W_1 , W_2 and W vanish. It is also clear that $W_1, W \ll W_2$ since only the exponential tail of the 1s state fall under the potential, whereas $\langle r \rangle = 6$ a.u. falls inside the cage wall for the 2s state. These overlaps depend on the position, the width, and the depth of the cage potential. For a given cage position and width, the matrix elements then become:

$$W_1 = U_0 K_1, \quad (23)$$

$$W_2 = U_0 K_2, \quad (24)$$

$$W = U_0 K, \quad (25)$$

where the cage depth U_0 is the only a parameter we vary. Here $K_1 \simeq 1.6 \times 10^{-3}$, $K_2 \simeq 0.5$, and $K \simeq -2.8 \times 10^{-2}$. Note that $K_1, |K| \ll K_2$ as expected. The hamiltonian in (16) now becomes

$$\begin{pmatrix} E_1 + W_1 & W \\ W^* & E_2 + W_2 \end{pmatrix} = \begin{pmatrix} E_1 + U_0 K_1 & U_0 K \\ U_0 K & E_2 + U_0 K_2 \end{pmatrix}. \quad (26)$$

We now consider how the eigenvalues of this matrix change as U_0 is varied. When U_0 is small enough such that the off-diagonal elements are much smaller than the diagonal elements, the matrix is essentially diagonal and E_1 and E_2 are shifted linearly for small values of U_0 (see Fig. 5). Since K_1 is also very small, $E_1 + U_0 K_1$ mainly remains unchanged and $E_2 + U_0 K_2$ decreases as U_0 is increased (as the cage deepens, recall that $U_0 = -|U_0|$). This is what we see for the $2s^*$ state in Fig. 5 until U_0 reaches ~ -70 eV.

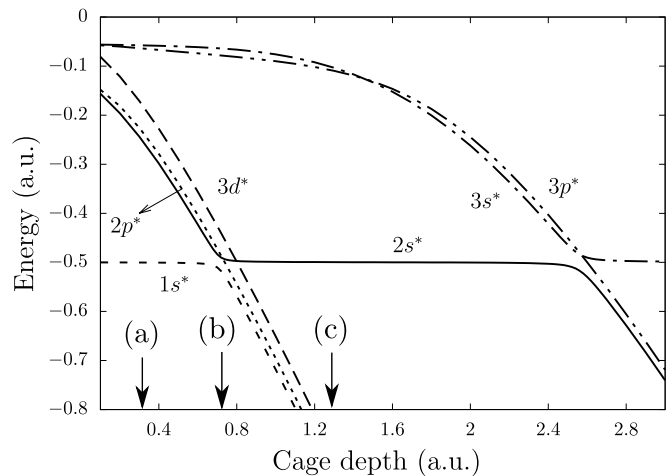


FIG. 5. (Color online) Energy level curves for the $1s^*$, $2s^*$ and $3s^*$ states of $H@C_{60}$ as a function of the cage depth U_0 . There are avoided crossings at $U_0 \sim 0.7$ a.u. between the $1s^*$ and the $2s^*$ states, and at $U_0 \sim 2.6$ a.u. between the $2s^*$ and the $3s^*$ states. States with different parity do not avoid each other. Three points in cage depth are labeled at (a) 0.3 a.u., (b) 0.7 a.u., and (c) 1.3 a.u..

Around ~ 0.7 a.u., the discriminator in Eq. (17) is large enough to give two distinct energies, E_+ and E_- , and

prevents the energies from becoming equal. Levels end up repelling each other. The size of the avoided crossing is $\Delta_{12} = |E_+ - E_-| = \sqrt{(E_1 - E_2 + W_1 - W_2)^2 + 4|W|^2}$. At this point, the eigenvectors switch roles and K_1 starts to behave like K_2 and K_2 like K_1 . As a result, as U_0 is decreased further, $1s$ starts to behave like $2s$ used to before the avoided crossing, and $2s$ starts to behave like the former $1s$. This is what we see in Fig. 5 from ~ 0.7 a.u. to ~ 2.6 a.u. This is reflected in the radial distributions of the states $1s^*$ and $2s^*$. As these states go through the avoided crossing in Fig. 5, the $2s^*$ state radial wave function starts to mimic the $1s$ state radial wave function (see Fig. 6). The radial states stay like these until the $2s^*$ state meets the $3s^*$ state at another avoided crossing around 2.6 a.u..

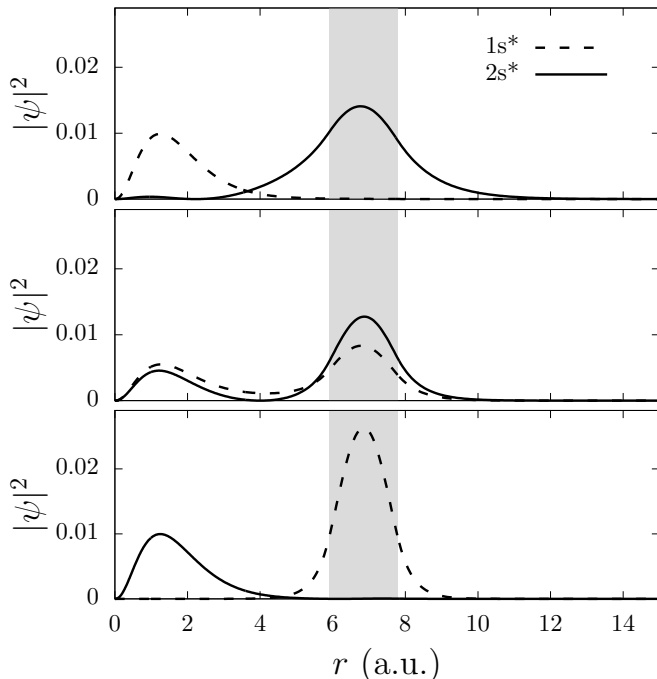


FIG. 6. (Color online) A figure showing the $1s^*$, $2s^*$ states of $H@C_{60}$ at three cage depths (labeled a, b, c in Fig.5) around the avoided crossing between these states. The cage depth is swept from top (a) to the bottom panel (b) in Fig.5. Before the avoided crossing the $2s^*$ state mainly localized on the cage wall, which moves to where the $1s^*$ state was localized after the avoided crossing.

The level crossings described above are responsible for three distinctly different regimes separated by the two avoided crossings seen in Fig. 5: (1) before the first avoided crossing at ~ 0.7 a.u., (2) between the two avoided crossings, and (3) after the second avoided crossing at ~ 2.6 a.u.. In simulations of HHG out of $H(2s^*)@C_{60}$, the depth of the fullerene cage is 0.3 a.u. which is labeled as (a) in Fig. 5. To demonstrate how the HHG spectra change as we vary the cage depth across the avoided crossing, we have performed simulations at two other cage depths at 0.7 a.u. and 1.3 a.u. labeled

as points (b) and (c) in Fig. 5. The radial distributions of the $1s^*$ and the $2s^*$ states at these three points are shown in Fig. 6. Before the avoided crossing at (a), the radial distribution of the $2s^*$ state is mainly localized on the fullerene cage wall and the $1s^*$ state is entirely inside. For the laser intensity of $5 \times 10^{13}/n^8$ W/cm² and wavelength $800n^3$ nm of these set of simulations, the ground state generates no higher harmonics.

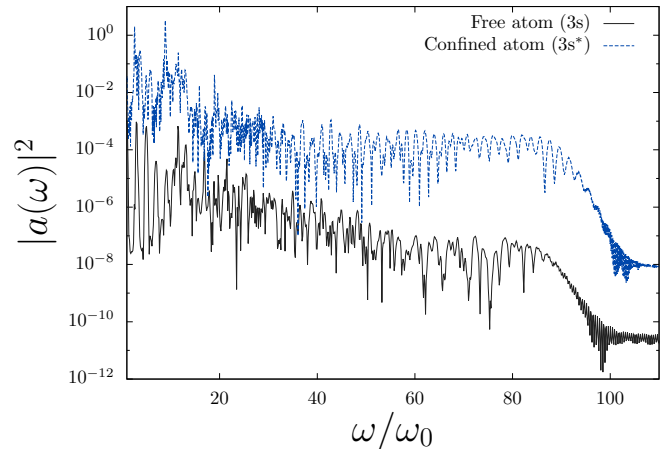


FIG. 7. (Color online) Harmonic spectra from free (black solid) and combined atom-fullerene systems (blue dashed) when they are initially prepared in the $3s$ and $3s^*$ states. The intensity and wavelength are $5.0 \times 10^{13}/n^8$ W/cm² and $800n^3$ nm where $n = 3$. The enhancement is seen by confining the atom inside the C_{60} shell is despite the fact that the $3s^*$ state is more deeply bound compared to the $3s$ state, and that there is $\sim 4\%$ ionization from the confined system whereas there is virtually no ionization from the free atom.

On the other hand, the $2s^*$ state generates very few harmonics with a much smaller cut-off frequency when compared with that from a free atom in the $2s$ state. This is again due to that fact that the $2s^*$ state can tunnel to either to the left or the right of the fullerene cage wall due to its radial localization. This severely reduces the amplitude of the tunneled wave packet that can effectively contribute to the HHG process. During the avoided crossing at (b), the $1s^*$ and the $2s^*$ states exchange their radial localization, while retaining their nodal structures. After the voided crossing at (c), the $2s^*$ state is localized essentially where the $1s^*$ state used to be. In this case, the binding energy of the state and the width of the tunneling barrier are too large for the $2s^*$ state and HHG is turned off completely. There is no effective HHG from the $2s^*$ state until after the second avoided crossing with the $3s^*$ state at ~ 2.6 a.u., after which the $2s^*$ state becomes localized on the cage again, and the harmonic spectra reverts to a spectrum similar to the one seen in the top panel of 4. The overall intensity of the generated harmonics decrease, however, since the $2s^*$ state becomes more deeply bound on the cage wall, and tunneling becomes progressively harder.

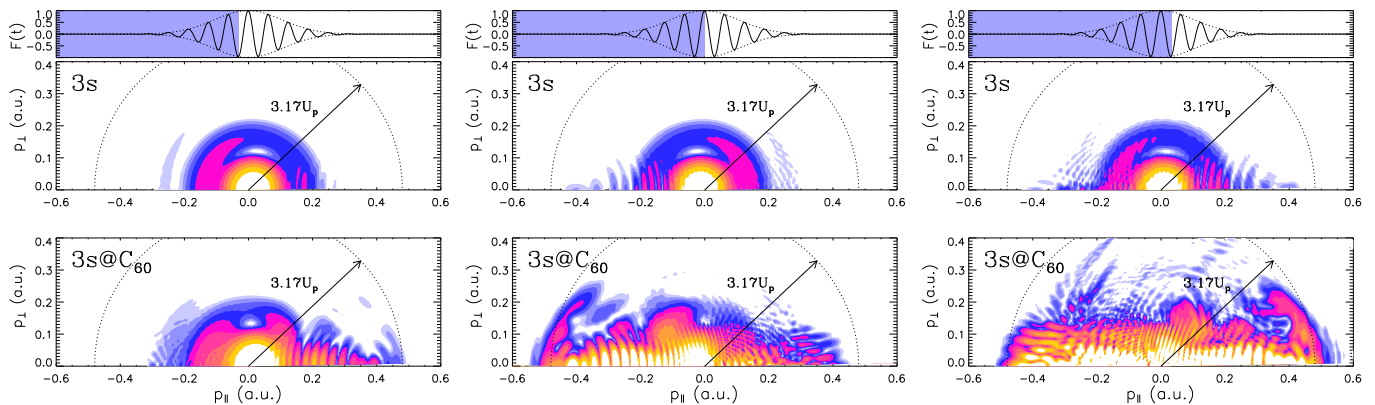


FIG. 8. (Color online) Time-dependent momentum distribution of the total wavefunction evaluated according to the method described in Sec. IID. The top row is for a free atom prepared in the $3s$ state at three specific points spanning one laser period at the peak of the laser pulse (indicated on top). The lower row shows the momentum distributions at the same instances during the pulse for $H(3s^*)@C_{60}$. The boundary which marks the kinetic energy corresponding to the cut-off frequency for a free atom at $3.17U_p$ is also indicated as a dashed semicircle in each case.

C. $H(3s^*)@C_{60}$

The most intriguing situation arose when we compared spectra from systems initially prepared in excited states whose classical turning points at $2n^2$ as well as $\langle r \rangle$ lie outside the fullerene shell. In this case, we see substantial enhancement from the atom-fullerene system compared to the spectra from a free H atom. Specifically, we report results for the $3s$ and $3s^*$ states here where the intensity and the wavelength are $5.0 \times 10^{13}/n^8$ W/cm² and $800n^3$ nm with $n = 3$. In the $3s^*$ state, the classical turning point is at ~ 18 a.u. and $\langle r \rangle \sim 13.5$ a.u., both of which are well outside the C_{60} shell. In this case, we see a drastic enhancement in the HHG yield from the combined atom-fullerene system by ~ 4 orders of magnitude compared to the free atom alone (Fig. 7). We see similar behavior for higher excited states as well, such as when we compare $4s$ and $4s^*$ states, which we do not report here. We should also note here that the enhancement seen in Fig. 7 does not disappear when we increase the intensity as was the case for HHG from the $1s^*$ state in Fig. 2. Comparing $\langle \dot{z} \rangle$ and $\langle \ddot{z} \rangle$, we see that the velocity form of the emitted power is larger than that obtained from the acceleration form by ~ 3 orders of magnitude throughout the plateau for both the free atom and the $H@C_{60}$ spectra.

The spherically symmetric potential creates a small phase shift in the radial part of the eigenstate and pulls the electron slightly towards the nucleus. This gives a more deeply bound $3s^*$ state, and the energies for the $3s$ and $3s^*$ states differ by $\sim 3.5\%$. Despite tunneling out of a more deeply bound state, the $H(3s^*)@C_{60}$ system emits a far more intense plateau of harmonic photons. On the other hand, there is virtually no ionization out of the $3s$ state whereas the ionization from $H(3s^*)@C_{60}$ is at the $\sim 4\%$ level. This also works towards reducing the HG yield from the combined $H(3s^*)@C_{60}$ system relative

to the yield from a free atom. To understand the origin of the enhancement seen in Fig. 7, first note that the enhancement throughout the plateau is essentially uniform, meaning that the enhanced emission yield at high-order harmonics has not come at the expense of the lower harmonics: there is enhancement throughout the plateau between ~ 2 -4 orders of magnitude. This suggests that the significant enhancement seen in Fig. 7 cannot result from a higher-order process where low order harmonics get converted up to higher harmonics. Furthermore, the existence of the fullerene shell cannot alter the dynamics of the tunneled wave-packet in the propagation step of the HHG process, which now happens well outside the C_{60} cage for the combined atom-fullerene system. Combined with the fact that the $H(3s^*)@C_{60}$ system effectively suffers from a smaller tunneling rate, the enhancement in Fig. 7 could only have come from the recombination step of the HHG process.

Comparing the momentum distributions for the free and the $H(3s^*)@C_{60}$ systems, we can gain insight into the key differences in the dynamics taking place in both cases to help elucidate the mechanism at play leading to enhancement. We evaluate momentum distributions at three instances during the laser pulse, which are shown in Fig. 8. We take these snapshots over a complete cycle of the laser field at the peak of the pulse envelope (shown on top). The top row is for the free atom, and the bottom row is from the combined atom-fullerene system. The first thing we notice is that in both cases the momentum is confined within a sphere in the momentum space with a radius corresponding to a kinetic energy of $3.17U_p$ (dashed circle). This aligns with the fact that both HHG spectra seen in Fig. 7 have the same cut-off frequency and no higher harmonics have been generated by confining the atom inside the fullerene. The second point is that there is a larger momentum spread in the p_{\perp} component for $H(3s^*)@C_{60}$ compared to the free atom momen-

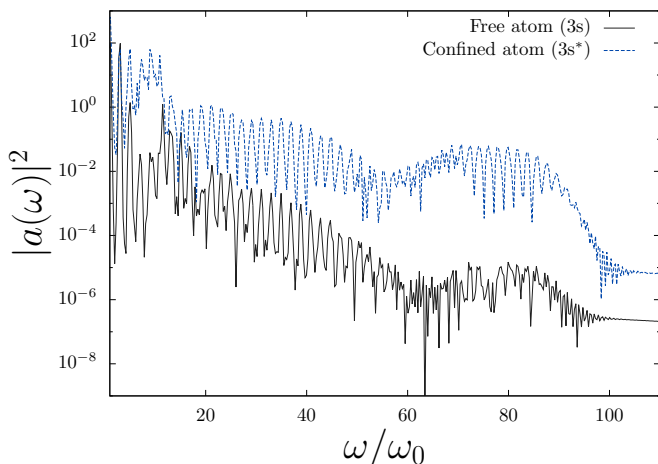


FIG. 9. (Color online) Same spectra reported in Fig. 7 except calculated using the Green’s function method described in Sec. II C for the same laser parameters discussed in the text.

tum distribution, which is important in understanding the origin of the enhancement seen in Fig. 7. The larger the momentum spread in the direction perpendicular to the laser polarization the smaller the spatial spread of the wavepacket in this direction, which would lead to a more efficient recombination process.

When the classical turning point of the initial state is well outside the fullerene shell, such as for states with $n \geq 3$, tunneling happens outside the C_{60} cage ($2n^2 > r_c$), but recombination happens inside (momentum conservation). This means, the outgoing wavepacket is identical to that from a free atom, but when it returns to its parent ion to recombine, it must go inside the shell and gets spatially squeezed along the direction of the laser polarization by the potential shell. The momentum distribution doesn’t exhibit higher momentum components compared to that for a free atom (Fig. 8), and the incoming wavepacket having a smaller spatial spread means a higher probability for recombination. This is why we do not see any higher harmonics generated in the confined case; the cut-off remains exactly where it was when the atom was free. However, the intensity of the emitted harmonics is increased, meaning that the momentum distributions remained essentially within the same sphere with a radius corresponding to the maximum kinetic energy of $3.17U_p$ in the momentum space. However, the recombination efficiency is enhanced. This is made further clear by the fact that no harmonics lost intensity compared with the free atom in Fig. 7, where all the harmonics are increased in intensity (or at least remained the same). This suggests that the effect cannot be due to a some of the harmonics getting converted into others. See Fig. 3 for all three distinct cases discussed.

It should be possible to see the lensing effect depicted in Fig. 3 leading to the enhancement in Fig. 7 by comparing the time-dependent probability current densities

(PCD) $|\psi(\mathbf{r}, t)|^2$ for H(1s) and H(3s*)@ C_{60} in space. The problem, however, is that only a small fraction of the total wavefunction contributes to the HHG process, and most of the amplitude sits where the initial state resides near the origin. The fullerene shell also lies in this region of space, and whatever interesting dynamics takes place here is buried underneath the initial amplitude, and therefore is not visible. One way around this difficulty is to use the Green’s function method described in Sec. II C. This is essentially the time-dependent perturbation theory in which we solve for the time-evolution of the first-order correction to the total wavefunction. This part of the wavefunction is what mainly contributes to the HHG process. Although no net photon absorption/emission takes place in the tunneling step of HHG, time-dependent perturbation theory can still describe tunneling if a time-dependent potential [25] enables it. The time-dependent perturbation theory is routinely used in calculating transmission/reflection coefficients at solid state junctions, and it gives accurate results. We also calculate the dipole acceleration using $\psi_1(\mathbf{r}, t)$ to ensure that the Green’s function method we use capable of capturing the relevant physics and see if it can reproduce the enhancement we see in Fig. 7.

We show the HHG spectra from H(1s) and H(3s*)@ C_{60} obtained using $\psi_1(\mathbf{r}, t)$ from Sec. II C in Fig. 9. The perturbative method we use qualitatively reproduces the drastic enhancement effect we see in Fig. 7. There is ~ 4 orders of magnitude enhancement for harmonics above $\omega/\omega_0 > 60$, and between 1-4 orders of magnitude enhancement for lower harmonics. For no harmonic in the plateau region, there is a reduction in the emitted photon intensity from H(3s*)@ C_{60} compared to the free atom. This implies that the physical mechanism responsible for the enhancement we see in Fig. 7 is captured in the Green’s function method in essence.

We plot the time-dependent PCD at four instances during the laser pulse in Fig. 10. The four snapshots span one laser cycle in the rising edge of the pulse as indicated on top for each time-frame. The left panels show the PCD for a free atom and right panels show that for the combined atom-fullerene system. The position of the spherically symmetric fullerene shell is marked by the dashed and solid circles in each case. Note that the PCDs are not synchronized in the snapshots because the binding energies for the 3s and 3s* states are slightly different, which translates into different tunneling times. It is clear from Fig. 10 that when the returning wavepacket arrives at the fullerene cage in the first frame, the transmitted part of the wavefunction is denser inside the cage (right) relative to the same for the free atom (right). This part of the wavepacket is revived on the opposite side of the atomic core inside the cage in the second half of the laser cycle (last frame). At no point during the laser cycle, the transmitted part of the wavepacket for the free atom is as densely focused along the laser polarization as the confined atom. This is again in line with the time-dependent momentum distributions we see in Fig. 8 which show

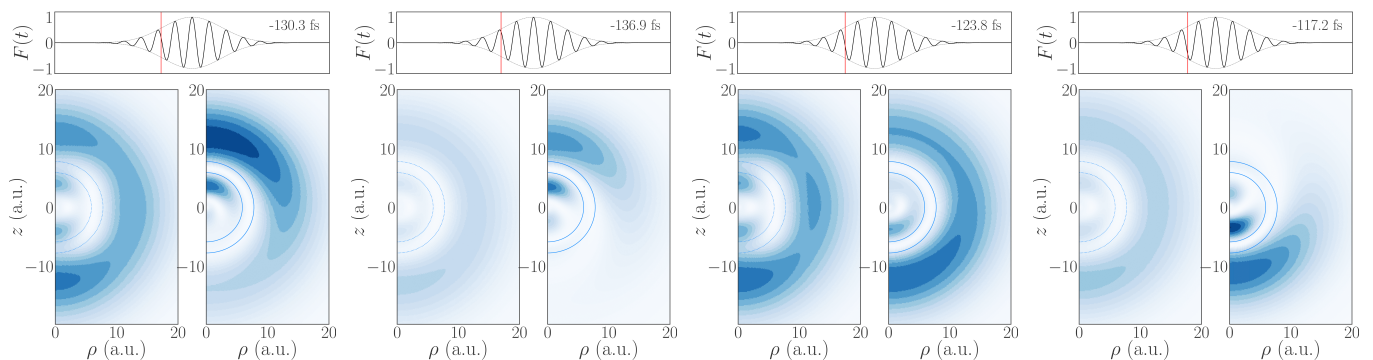


FIG. 10. (Color online) Wavefunction plots showing the squeezing of the returning wave packet before recombination for HHG out of $n = 3$. Each snapshot contains two panels. The panels on the left show the PCD from H(1s), and the panels on the right show the PCD from the H(3s*)@C₆₀ system. The position of the fullerene shell is marked by dashed (free atom) and solid (confined) blue semicircles in each panel. The snapshots are taken over a complete laser period instances of which we indicate on top of each time-frame.

a much broader spread of momentum in the direction perpendicular to the laser polarization for H(3s*)@C₆₀. A larger spread in momentum translates to a narrower spread in space.

We also want to make the point that the atoms inside a real C₆₀ are not centered as they are in our model, but are off-centered, and typically situated near the inner wall of the fullerene. Accurately reflecting this would affect our results. However, a real experiment is performed on a macroscopic ensemble of atoms, such as a gas jet. A uniform distribution of positions of atoms inside C₆₀ cages would produce a macroscopic response that is closely mimicked by a response obtained from our model simulations where the atom is assumed to be centered. This is because, in the absence of non-linearities, such as substantive ionization, the macroscopic response can be qualitatively reproduced by averaging single atom responses from atoms inside the gas. This is why, for example, numerical data for photoionization of C₆₀ using this kind of model potentials agree so well with data from experiments in the literature (see, e.g., [22, 26, 27]). The reason for this is that although the calculations assume that the atom is centered at the origin, the experiment is performed on a gas target which contains a large number of atoms, and that what is measured is the macroscopic response.

IV. FUTURE DIRECTIONS

What we have demonstrated here is that coupling atoms to nanostructures can significantly enhance HHG yield. However, we have used a hydrogen atom for this purpose chiefly because of the lower intensities need to extract high-harmonics from it while keeping depletion of atoms due to ionization to a minimum. Furthermore, the fullerene cage coupled to the H atom easily fragments through a multi-photon ionization process in intensities

typical for HHG using noble gas atoms in experiments. The question is then how this could be made into a useful tool in the laboratory.

The issue of fragmentation of the fullerene cage is partly alleviated by realizing that even though a significant fraction of the fullerene cages are destroyed in intensities typical for noble gas atoms well before the peak of the driving laser pulse is reached, even a small fraction of the initial fullerene population surviving would mean a significant enhancement in the overall macroscopic response of the medium. This is due to the fact there are ~ 4 orders of magnitude enhancement in the response from the confined species in Fig. 7. Even if $\sim 1\%$ of the Ne@C₆₀ or Ar@C₆₀ populations survive the peak of the laser pulse, there will still be a substantial increase in yield in the macroscopic response if the medium initially starts with endohedral fullerenes.

To assess what fraction of the initial endohedral fullerenes needs to survive the laser pulse for a meaningful increase in the yield, one needs to propagate the generated harmonics through the mixed medium consisting of atoms and endohedral fullerenes to obtain the final macroscopic response. Using experimental data available, such as those reported in Ref. [20], one can evaluate what laser intensities are optimal that can maximize the high-harmonic photon yield while keeping fragmentation rate to a minimum to obtain a meaningful enhancement in the macroscopic spectrum. One issue that needs attention here is that large ionization rate from the fullerenes will alter the dispersion characteristics of the macroscopic medium. Therefore it is important to take a significantly modified refraction index of the medium into account due to the hot carbon plasma generated from fragmentation of the fullerenes. This means it is also necessary to propagate the fundamental laser pulse in parallel with the generated harmonics. It would be interesting to understand how phase-matching works in this case, where the medium is gradually stripped from the endohedral

fullerenes down to an environment consisting of atoms inside an ionized carbon plasma dispersing the generated harmonics.

There are other demonstrated mechanisms which can potentially be used to enhance the HHG yield. One example of this is has been demonstrated using plasmonic effects [11–14]. Because the physics is different in both cases, these can be combined to obtain enhancement from two physically independent processes. Another example is preparing the initial atom in a superposition state involving the ground and an excited state [28, 29]. Coupling the ground state to a Ry state also increases HHG efficiency, partly because the Ry electron can tunnel more efficiently than the ground state, and the returning wavepacket preferentially recombines back into the state out of which it tunneled.

As one needs intense and high harmonics for applications, such as in attosecond pulse generation, ground state atoms are usually preferred in HHG rather than

the excited states. One can start with a superposition state of the combined atom-fullerene system, like $(|1s^*\rangle + |3s^*\rangle)/\sqrt{2}$, would give enhancement over to using just the ground state. Furthermore, it may be interesting to see how all these different enhancement mechanisms, *e.g.* plasmonic effects, superposing with a Ry state, and confinement can compound to give an enhanced yield in the macroscopic response of a gaseous target.

V. ACKNOWLEDGEMENT

TT was supported in part by the National Science Foundation (NSF) Grant No. PHY-1212482 and acknowledges the use of UNR Grid Cluster for simulations. EAB was supported by BAPKO of Marmara University Grant No. FEN-A-071015-0477. EAB also thanks Mr. Dogan Bolak for providing additional computational resources.

-
- [1] M. Lein, *Journal of Physics B: Atomic, Molecular and Optical Physics* **40**, R135 (2007).
 - [2] M. Hentschel, R. Kienberger, C. Spielmann, G. a. Reider, N. Milosevic, T. Brabec, P. Corkum, U. Heinzmann, M. Drescher, and F. Krausz, *Nature* **414**, 509 (2001).
 - [3] Y.-Y. Yang, Q.-G. Li, L. Zhang, and X.-C. Lin, *Plasmonics* (2015), 10.1007/s11468-015-0010-7.
 - [4] F. McGrath, P. Hawkins, E. Simpson, T. Siegel, Z. Diveki, D. Austin, A. Zair, M. Castillejo, and J. P. Marangos, *Proc. SPIE 8984, Ultrafast Phenomena and Nanophotonics XVIII* **89841B** (2014), 10.1117/12.2039123.
 - [5] S. Pabst and R. Santra, *Phys. Rev. Lett.* **111**, 233005 (2013).
 - [6] A. D. Shiner, B. E. Schmidt, C. Trallero-Herrero, H. J. Wrner, S. Patchkovskii, P. B. Corkum, J.-C. Kieffer, F. Lgar, and D. M. Villeneuve, *Nature Physics* **7**, 464467 (2011).
 - [7] M. B. Gaarde, F. Salin, E. Constant, P. Balcou, K. J. Schafer, K. C. Kulander, and A. L’Huillier, *Phys. Rev. A* **59**, 1367 (1999).
 - [8] P. Salières, P. Antoine, A. de Bohan, and M. Lewenstein, *Phys. Rev. Lett.* **81**, 5544 (1998).
 - [9] P. Antoine, D. B. Milošević, A. L’Huillier, M. B. Gaarde, P. Salières, and M. Lewenstein, *Phys. Rev. A* **56**, 4960 (1997).
 - [10] E. J. Takahashi, T. Kanai, K. L. Ishikawa, Y. Nabekawa, and K. Midorikawa, *Phys. Rev. Lett.* **99**, 053904 (2007).
 - [11] A. Husakou, S.-J. Im, and J. Herrmann, *Physical Review A* **83**, 043839 (2011), arXiv:1009.4124.
 - [12] S. Kim, J. Jin, Y.-J. Kim, I.-Y. Park, Y. Kim, and S.-W. Kim, *Nature* **453**, 757 (2008).
 - [13] I. Yavuz, E. A. Bleda, Z. Altun, and T. Topcu, *Physical Review A* **85**, 013416 (2012).
 - [14] M. F. Ciappina, J. Biegert, R. Quidant, and M. Lewenstein, *Physical Review A* **85**, 033828 (2012).
 - [15] P. B. Corkum, *Physical Review Letters* **71**, 1994 (1993).
 - [16] T. Topcu and F. Robicheaux, *Physical Review A* **86**, 053407 (2012).
 - [17] E. a. Bleda, I. Yavuz, Z. Altun, and T. Topcu, *Physical Review A* **88**, 043417 (2013).
 - [18] T. Topçu and F. Robicheaux, *Journal of Physics B: Atomic, Molecular and Optical Physics* **40**, 1925 (2007).
 - [19] A. Jaroń-Becker, A. Becker, and F. H. Faisal, *Physical Review Letters* **96**, 2 (2006).
 - [20] S. Hunsche, T. Starczewski, A. l’Huillier, A. Persson, C.-G. Wahlström, H. B. van Linden van den Heuvell, and S. Svanberg, *Phys. Rev. Lett.* **77**, 1966 (1996).
 - [21] M. F. Ciappina, A. Becker, and A. Jaroń-Becker, *Physical Review A - Atomic, Molecular, and Optical Physics* **78**, 1 (2008).
 - [22] V. K. Dolmatov, G. T. Craven, E. Guler, and D. Keating, *Physical Review A - Atomic, Molecular, and Optical Physics* **80**, 1 (2009), arXiv:0908.2241.
 - [23] Y. Ni, S. Zamith, F. Lépine, T. Martchenko, M. Kling, O. Ghafur, H. G. Muller, G. Berden, F. Robicheaux, and M. J. J. Vrakking, *Phys. Rev. A* **78**, 013413 (2008).
 - [24] A. D. Bandrauk, S. Chelkowski, D. J. Diestler, J. Manz, and K. J. Yuan, *Physical Review A - Atomic, Molecular, and Optical Physics* **79**, 1 (2009).
 - [25] H. J. Reittu, *American Journal of Physics* **63**, 940 (1995), <https://doi.org/10.1119/1.18037>.
 - [26] A. Miller, S. Schippers, R. A. Phaneuf, M. Habibi, D. Esteves, J. C. Wang, A. L. D. Kilcoyne, A. Aguilar, S. Yang, and L. Dunsch, *Journal of Physics: Conference Series* **88**, 012038 (2007).
 - [27] Z. Chen, R. A. Phaneuf, and A. Z. Msezane, *Journal of Physics B: Atomic, Molecular and Optical Physics* **43**, 215203 (2010).
 - [28] Z. Zhai, Q. Zhu, J. Chen, Z.-C. Yan, P. Fu, and B. Wang, *Phys. Rev. A* **83**, 043409 (2011).
 - [29] Z. Zhai, J. Chen, Z.-C. Yan, P. Fu, and B. Wang, *Phys. Rev. A* **82**, 043422 (2010).